

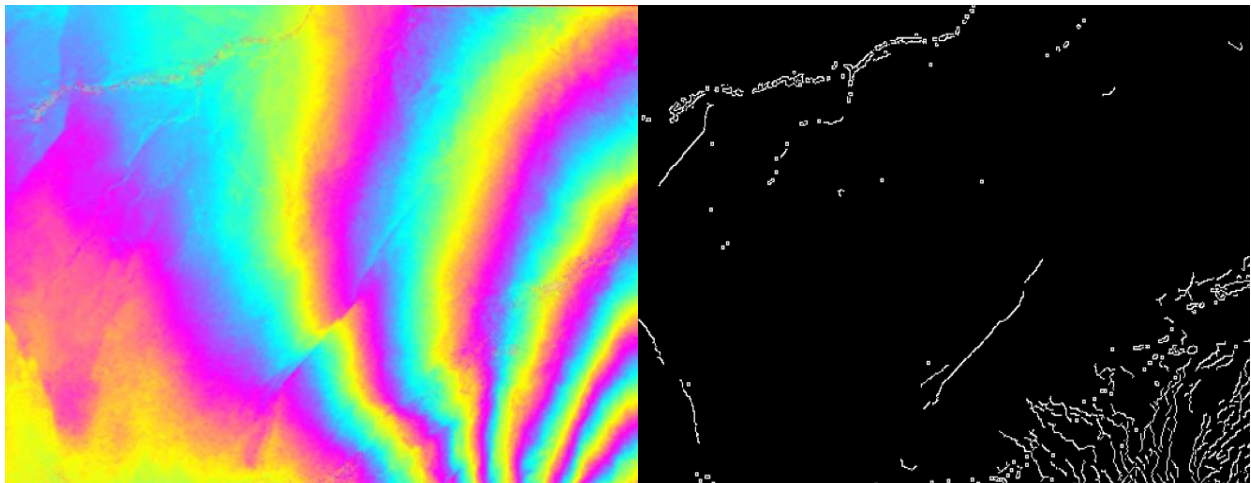
NASA DEVELOP National Program



Jet Propulsion Laboratory
Summer 2013

California Disasters

Detecting Undiscovered Faults in Southern California using
Computer-Vision Techniques and Uninhabited Aerial Vehicle
Synthetic Aperture Radar (UAVSAR) Interferometry



Technical Report

August 7, 2013

Christine Rains, California State University, Northridge (Project Lead)
Wesley von Dassow, Lafayette College
Magali Barba, California State Polytechnic University, Pomona
Margaret Glasscoe, Jet Propulsion Laboratory (Science Advisor)
Jay Parker, Jet Propulsion Laboratory (Science Advisor)

Abstract

Knowing the location and behavior of active faults is essential for earthquake hazard assessment and disaster response. In Interferometric Synthetic Aperture Radar (InSAR) images, faults are revealed as linear discontinuities. Currently, interferograms are manually inspected to locate faults. During the summer of 2013, the NASA-JPL DEVELOP California Disasters team contributed to the development of a method to expedite fault detection in California using remote-sensing technology. The team utilized InSAR images created from polarimetric L-band data from NASA's Uninhabited Aerial Vehicle Synthetic Aperture Radar (UAVSAR) project.

A computer-vision technique known as "edge-detection" was used to automate the fault-identification process. This project tested and refined an edge-detection algorithm under development through NASA's Earthquake Data Enhanced Cyber-Infrastructure for the Disaster Evaluation and Response (E-DECIDER) project. To optimize the algorithm both UAVSAR interferograms and synthetic interferograms generated through *Disloc*, a web-based modeling program available through NASA's QuakeSim project, were used. The initial study focused on earthquake faults that revealed themselves through coseismic and post-seismic displacements in the Imperial Valley, California, relative to the April 4, 2010, El Mayor-Cucapah earthquake in Baja California, Mexico. Using an edge-detection code and both synthetic and UAVSAR data-based interferograms, the team contributed to the development of an automated methodology to quickly process interferometric data, allowing the identification of motion along known and unknown faults in a large area to proceed in an efficient manner. The results of the methodology were compared with fault data from other studies on El Mayor-Cucapah-earthquake-related faulting and found to be comparable.

The algorithm detected seismic, aseismic, and coseismic slip along faults that were identified and compared with databases of known fault systems.

This optimization process was the first step toward integration of the edge-detection code into E-DECIDER to provide decision support for earthquake preparation and disaster management. E-DECIDER partners that will use the edge-detection code include the California Earthquake Clearinghouse and the US Department of Homeland Security through delivery of products using the Unified Incident Command and Decision Support (UICDS) service. Through these partnerships, researchers, earthquake disaster response teams, and policy-makers will be able to use this new methodology to examine the details of ground and fault motions for moderate to large earthquakes. Following an earthquake, the newly discovered faults can be paired with infrastructure overlays, allowing emergency response teams to identify sites that may have been exposed to damage. The faults will also be incorporated into a database for future integration into fault models and earthquake simulations, improving future earthquake hazard assessment. As new faults are mapped, they will further understanding of the complex fault systems and earthquake hazards within the seismically dynamic state of California.

Keywords

Remote-Sensing, Fault-detection, Interferometry, UAVSAR, Edge-detection, Earthquake Disaster

Introduction

Background Information

Knowing the location and parameters of current active faults in California, one of the most seismically active states in the United States, is essential to earthquake hazard assessment. Moreover, knowing where a fault has ruptured and the deformation it has caused following an earthquake is essential for earthquake disaster response. California recently experienced an earthquake that highlighted the need for knowing the location of active faults. On April 4, 2010, the moment-magnitude 7.2 El Mayor-Cucapah (EMC) earthquake rattled Southern California. Although the epicenter of this quake was in Baja California, interferograms developed within weeks of this earthquake revealed both the motion of main fault and coseismic motion in a network of neighboring faults in both Mexico and California. Radar interferometry discovered that the main shock caused ruptures of the Borrego and Pescadores faults, faults that had been mapped but were considered inactive (Wei et al.). Furthermore, radar interferometry revealed triggered slip on neighboring faults, most of which were unmapped (Wei et al.). Subsequent radar studies of the area revealed continued motion during the next several months due to gradual stress redistribution and aftershocks. Thus, the El Mayor-Cucapah earthquake reaffirmed the effectiveness of using radar interferometry to detect faults.

Radar interferometry is becoming a more widely employed method for fault detection. Interferograms constructed from radar data obtained by satellites or airplanes have been used to detect and quantify ground changes or ground motion remotely over large areas since the late 1990's. Currently, interferograms are manually inspected to locate faults that are affected by an event. In an effort to decrease the time it takes to scan UAVSAR interferograms, Dr. Parker of NASA's Jet Propulsion Laboratory has developed an edge detection algorithm to automate the fault detection process. In collaboration with Dr. Parker, the DEVELOP California Disasters Team was tasked to improve the performance of the edge detection algorithm, to further demonstrate its use in detecting fault features, and to create detailed risk assessment maps of the study areas.

Synthetic Aperture Radar data from the Unmanned Aerial Vehicle Synthetic Aperture Radar (UAVSAR), one of NASA's Earth Observation Systems (EOS) was downloaded for use. This data was taken from a database maintained by QuakeSim, an online computational infrastructure self-described as "a project to develop a solid Earth science framework for modeling and understanding earthquake and tectonic processes" (2011). UAVSAR is mounted on a NASA-operated Gulfstream GIII aircraft and consists of an array of active radar sensors that pulse L-band frequency ($f=1-2$ GHz; $\lambda=15-30$ cm) waves at a target (Toan, 2007). The aperture ("antenna") size directly affects the resolution of the image created. By combining echoes from multiple radar pulses, an "antenna" longer than the physical sensor itself is synthesized, allowing higher resolution images to be created than would be possible for other radar instruments of comparable size (Rosen, 2008). Radar in this frequency (L-band) is powerful because it is insensitive to clouds, light rain, nor foliage (Toan, 2007). The "tube's" size is such that flight-path discrepancies can be processed out of the raw data later. Additional discrepancies based on airplane tilt are accommodated by steering the antenna array independently of the aircraft. UAVSAR capitalizes on these attributes by flying the same path within a 10-meter diameter "tube" at two moments in time. By "interfering" the

data, processing the phase measurements of these two images in concert, the result is precise data on ground surface movement with sensitivity on the millimeter-resolution scale. This data is representative of changes that have occurred during the time period between the two images in the distance from the UAVSAR instrument to the ground, making UAVSAR a valuable tool for studying earthquake events.

Radar interferometry has proven useful for fault detection, but significant issues remain preventing the automated exploitation of the data. An example issue with automated fault detection is “white noise” in the fault maps produced by the algorithms. Features such as dry riverbeds, highways, and roads in the radar data result in false positives in the fault maps. To fully automate the edge-detection code, the white noise will need to be removed to produce a fault map where the only edges detected correspond to surface fault traces.

Project Objectives

The main objective was to utilize UAVSAR-derived interferograms as well as modeled synthetic interferograms to test and optimize the edge-detection algorithm. In the testing and optimization process, the faults identified in the UAVSAR interferograms are to be compiled into a small database of faults. Using the detected faults, synthetic interferograms will be produced as inputs into E-DECIDER to create tilt and deformation maps. The tilt and deformation maps, along with infrastructural and demographic data, will be utilized to create a risk assessment map.

Study Area

The study focused initially on a small area of the Imperial County in Southern California.

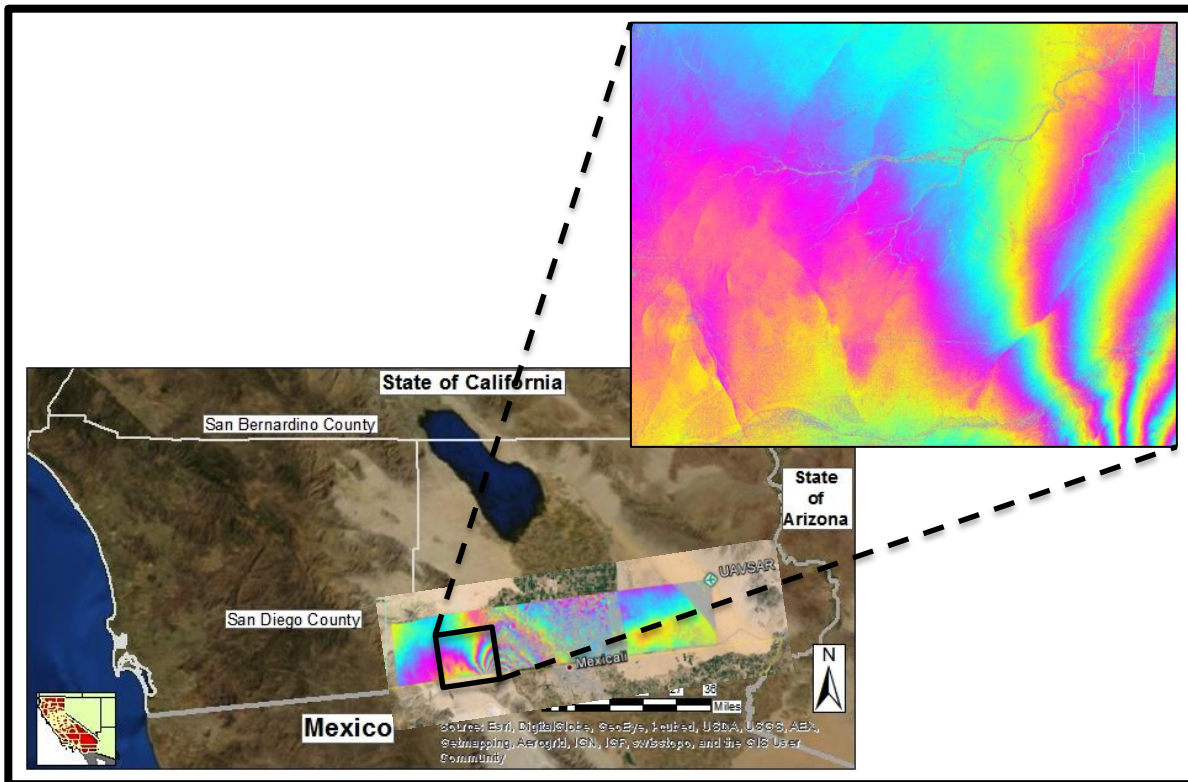


Figure 1. Interferogram of case study area in Imperial Valley, Southern California.

This study area was chosen because it contains the highest density of UAVSAR coverage of the 2010 El Mayor-Cucapah Earthquake. The San Diego and Imperial Counties also have a general high earthquake hazard. The areas provide a suitable context to test the development of this edge detection algorithm against features that are well studied in established literature. The spatial polygon used as a case study for parameter variation was defined by latitude/longitude points: 32.733822, -115.858172; 32.733822, -117.728489; 32.653908, -115.728489; 32.653908, -115.858172. This area will be referred to as PolySel2 from this point forward. InSAR from other areas of California were observed, but not utilized extensively.

Study Period

During the initial stage of the project, UAVSAR data from October 21, 2009 and April 13, 2010 was used to study the April 4, 2010 El Mayor-Cucapah Earthquake. Once this method was mostly established, UAVSAR data from several time periods between 2007 and 2013 was employed.

National Application Addressed

This project addresses NASA's Natural Disasters application area of the national Applied Sciences Program by utilizing remote sensing data from NASA's Earth Observing System (EOS), modeling techniques, and analysis to aid geohazard preparation and response.

Project Partners

The California Earthquake Clearinghouse (CEC) serves to provide a temporary organization following an earthquake disaster to coordinate field investigations, facilitate the dissemination of knowledge produced by and for, emergency responders, engineering, and scientific communities. The Clearinghouse is composed of five state and national agencies as well as numerous member organizations whose collective goal it is to cooperate and share data, information, and expertise following damaging earthquakes. The edge-detection tool will provide critical deformation information to the CEC, which can then be used by its members in their response efforts following a large earthquake.

Science Applications International Corporation (SAIC) provides disaster mitigation, response, and recovery services to local governments, private and non-profit organizations, state-governments, public utilities, and universities. In relation to earthquake disasters, SAIC provides the Unified Incident Command & Decision Support (UICDS) software delivery system for decision support products to California state emergency operations. UICDS is a data-sharing framework constructed as part of the Department of Homeland Security's Initiative for Information Sharing among Commercial, Government, Academic, and Volunteer Technology Providers to Support the National Incident Management System.

Methodology

The data used in this project were produced in two fundamentally different ways: multiple-pass UAVSAR and Quakesim Disloc3 modeling. The acquisition of these two data types was different as was the processing needed to convert each into the text formatting read by the edge detection code (hedge2lt.py).

The UAVSAR data used was provided with prior processing to levels 1.1 and 1.5 done by NASA's Jet Propulsion Laboratory. Level 1.1 processing implies that the data has been compressed in both range and azimuth in slant range geometry (Alaska Satellite Facility). The Level 1.5 processing label implies that the data has been projected to map coordinates either by geo-referencing or geo-coding (Alaska Satellite Facility). The UAVSAR data used was collected from two primary sources: the UAVSAR Data Search tool on the uavsar.jpl.nasa.gov website and the InSAR Profile Tool on the QuakeSim.org website. The files needed from each swath include a metadata file (.ann), a correlation data file (.cor.grd), an unwrapped phase data file (.unw.grd), and an unwrapped phase image (unw.kmz).

UAVSAR data was converted into a format readable by the edge detection script (hedge2lt.py). To do this, a second script was employed (sar2simplex.py) which output three text files from the input UAVSAR data: the primary edge input and two secondary (index and summary) text files necessary to run the edge detection script.

The sar2simplex.py script outputs two secondary files (index and summary) that the edge script needs along with the primary output of the script in simplex format (Figure 2). An option for the script is specifying a user-defined KML polygon to define a smaller area within the swath for which the script will output data.

```
7 -30.932357 -18.986025 -4.709247 1.000000 37.799637 -5.319699
7 -30.916795 -18.986025 -4.782592 1.000000 37.797141 -5.319699
7 -30.901232 -18.986025 -4.761843 1.000000 37.794644 -5.319699
```

Figure 2. An example of Simplex formatting. Each row represents (from left to right): type (radar), x (km), y (km), LOS displacement, uncertainty, elevation angle (degrees), azimuth (degrees).

The script has the ability to perform a few other functions as well, but they were not used. The optional KML region can be defined by creating a polygon on top of the interferogram (KMZ) in Google Earth and saving it to the folder where scripts and UAVSAR data are stored.

Data produced by the QuakeSim Disloc3 deformation model is the result of a series of input parameters (Figure 3).

Name	X	Y	Start Lat (°)	Start Lon (°)	End Lat (°)	End Lon (°)	Strike (°)	Dip (°)	Depth (km)	Width (km)	Length (km)	Strike Slip (mm)	Dip Slip (mm)	Lame Lambda	Lame Mu
TEST	6.9	0.0	34.1	-11	34.1	-11	-40	90.1	10.1	10.1	10.1	800	-10	1.0	1.0

Figure 3. Photo taken from Disloc portal of the input parameters needed to model a fault.

Running the model produces a synthetic interferogram image with a text file output of yet another form (Figure 4).

```
80 85 34.039795 -118.139763
6.981 0.023 -40.677
10.000 90.000 1.000 1.000 800.000 -10.000 0.000 10.675 10.000
x y ux uy uz exx exy eyy
-20.000 -22.000 7.607e-01 -5.318e+00 -5.361e-01 -2.703e-01 -1.300e-01 1.221e-01
```

Figure 4. This image is an example of a disloc output text file.

The Disloc3 data must then be converted into a "simplex" text format including all of the parameters necessary for the edge detection script to run. This is done by a script (dis2los.py) that calculates line of sight for the data along with elevation angle and azimuth for a fake airplane that is imagined to be collecting the data in the defined area, much as UAVSAR would. This script (sar2simplex.py) also outputs the two secondary text files that the edge detection script requires to run. The edge detection script (edgar.py) can be run using the primary inputs in simplex format and the two supporting files (index and summary). The edge detection script outputs four images and two histograms. The primary output is the "edgemap.png" image that outlines the detected edge. The three additional images are variations of "raw" images of the swath and the two text files of histogram data.

For visual analysis, "edgemap.png" was imported into ArcMap to be georeferenced to the .kml polygon from which it had been defined. This raster, now a layer, was then output as a .kml file so that it could be visually assessed compared to the interferogram and satellite imagery of the region it covered in Google Earth. In this way visual assessment was done comparing detected edges to the evident faults in the interferogram image.

To refine the effectiveness of the edge detection script (edgar.py) multiple parameters were manipulated within the script to monitor how they affected the resultant edge map. The primary parameters manipulated included the high threshold, lower threshold, smoothing coefficient (sigma_for_presmooth), and aperture size. Other parameters that exist in the script include Gaussian die-off, threshold ratio, scale, minimum value (valmin), and "fraction_pixels_not_edges"; however, they were found not to affect the performance of the algorithm.

For a large portion of the refinement of the edge detection script a single UAVSAR image was used. This area had been identified for the purpose of research by Dr. Jay Parker of NASA's Jet Propulsion Laboratory. It was established as a control for the known features, including faults, it contained as a reference to the edge script's output images. This image was a time series interferogram (SanAnd_26501_09083-010_10028-000_0174d_s01_L090HH_01) in the area of the El Mayor-Cucapah earthquake that occurred on April 4, 2010. The two images from which the interferogram was produced were taken on October 21, 2009 at 12:21 AM UTC and April 13, 2010 at 5:39 PM UTC.

As the edge script was refined, this method was confirmed in application to other InSAR imagery.

Fault maps, or edge maps, were georeferenced to the polygon from which they were created using the georeferencing tool in ArcMap. This allowed us to extract the exact latitude/longitude coordinates of the start and endpoint of the identified fault. This was then put into E-DECIDER's KML Generator service to create a risk assessment map. This file was then opened in Google Earth to reveal the infrastructure potentially affected (within a defined radius) by the activity along the fault.

Results & Discussion

Analysis of Results:

UAVSAR-Derived Data Results:

The deformation being detected by the edge detection algorithm is expressed as a line across which there is jump in values. This is because the features, faults, which

are being targeted, appear as a linear trace in the image due to the nature of the intersection of a fault plane with the ground surface. In an InSAR image, faults appear as a “tear in the fabric” of the image (Figure 5 – see appendix for figures 5 - 21). Other detected features that are non-faults are often polygonal or circular as they have two sides or edges along which the algorithm will detect a jump in values correlating to an edge. The script is set so that as differences in data values from one pixel to the next exceed a threshold, the script will recognize that as an edge and mark it as a positive output. From that point the script will attempt to extend the line in both directions from the initial point. Although these values may not exceed the upper threshold, the script will continue creating a line until values fall below a second, lower threshold.

The first parameter that was manipulated within the detection algorithm was the high threshold. The default value for high threshold is set to “ $0.013*255*2.0*1.5$ ” or 9.945. The default value produced results with more noise in the image than is desirable, thus this value is increased to reduce noise (Figure 6). The data values are scaled between 0 and 255 (grayscale), but since the range of values within the data set are not identical there is no standard or normalization for the grayscale values. As a result, the effect that changing the high threshold has on each UAVSAR image or polygon varies. Through testing different data and settings we have found that the scaling of data values done by the script may be flawed. Evidence of this is the fact that some images have shown that setting the high and low thresholds can yield a positive return in the scaled dataset. Additionally, there’s evidence that changes within the output occur when the high threshold is set above 255, which is theoretically the highest value any data point could have after scaling has been done.

The effect that the lower threshold has on edge detection was demonstrated to match what theory would dictate. That is to say that when the lower threshold was changed from its default value (50% of the high threshold) the edges detected would directly change in length i.e. a higher low threshold would shorten the length of edges (Figure 7).

Changing the smoothing coefficient (`sigma_for_presmooth`) created a similar effect in edges detected (Figure 8). Sigma was limited to relatively small values of roughly 1 to 10, the varying of which would produce significant differences in edge detection. Increasing the smoothing coefficient would eliminate small features and act to reduce the length of, or segment, long edges.

The final parameter manipulated with success was the aperture. This parameter deals with the averaging of pixel values to eliminate data dropouts and reduce the effects of extreme values. Raising the aperture (fixed to 3, 5, or 7 values) causes large, contour-like patterns to appear in the edge maps (Figure 9). This effectively requires that thresholds be set much higher to attain the same effect as with a lower aperture, but seems to reduce the noise present with the other parameters optimized (Figure 11).

After the California Disasters team tested the UAVSAR and synthetic interferograms with various parameters and shared the resulting edge maps, Dr. Parker added a function to output an image displaying the log of the magnitude of the phase gradient to the outputs of the edge detection code. This provided a visualization of, essentially, the data that was being processed by the edge detection script (Figure 12). What was found in the gradient map was that the river features have higher values than the faults themselves. This makes it impossible to isolate just the faults in the image without somehow dealing with the data having higher values than the faults. This would

likely involve the creation of a third threshold above the current upper threshold or some other data manipulation.

InSAR does not immediately discriminate between creep, triggered slip, or earthquake ruptures. However, the time frame in which displacements become visible to InSAR can be an indicator for interpretation of what kind of motion has occurred. Creep happens slowly and therefore does not readily appear in interferograms over short time scales. For example the creeping segment of the San Andreas Fault has a 387 day time period showing the creeping motion of the San Andreas Fault (Figure 13). Because of the extended time period between data acquisitions and the high creep rate, the right-lateral creeping motion is captured by the interferogram as a distinct line. Unfortunately, large time intervals between data acquisition result in higher incoherence between images resulting in large data dropouts during interferometric processing (Figure 14). Although it should have been easy to detect an edge from this image a lot of noise was the end result. Due to the large data dropout, the edge-detection code has trouble detecting the creeping segment of the San Andreas Fault in the image.

Another issue that presented a struggle throughout the summer was the inconsistency of the edge detection tool in producing results of similar quality from one swath area to the next. For example, a single polygon from a coseismic swath following the EMC earthquake was used for many tests as a control or reference point for variation. This was in part necessary because from polygon to polygon, data scaling done by the edge code would change causing the results produced by the image, and the amount of noise, to change significantly. To correct for the inconsistency, a later version of the fault edge detection algorithm was revised to scale thresholds roughly uniformly. This version of the code also defaults the aperture to 7, as opposed to the previous 3, and the low threshold ratio to 75%, as opposed to 50%, of the high threshold. The higher aperture has been deemed favorable at this point, although it forces the threshold higher, and the higher threshold ratio should decrease the amount of noise in the images even though it may decrease the length of faults detected.

Synthetic Data Results:

Disloc3 was used to answer questions on whether fault detection was affected by physical fault parameters and the line of sight (LOS) of the aircraft. This was possible because Disloc3 creates and analyzes data with respect to LOS, elevation angle values, and physical fault parameters to create a synthetic interferograms (Figure 15). Tested physical parameters included fault displacement (Figure 16 , 17), fault orientation (strike relative to LOS) (Figure 18), and fault type (normal, thrust, strike-slip) with respect to threshold values. Results of this process revealed that fault orientation had an effect on the pattern of noise produced in a disloc output. This was true even for faults that had been isolated by optimizing the threshold for a given image, if the orientation of the fault was changed for the same parameters, noise may reappear in the image. There were distinct patterns of noise that arose from the disloc model which did not mirror patterns of noise found in UAVSAR data. This is what one would expect to some degree; however, it does create a certain amount of uncertainty as to how much one can generalize these results to real data. Results in relation to displacement values were quite direct. The greater the displacement value, the larger a threshold had to be to isolate the fault trace and eliminate the background noise in the image. In these cases, noise also culminated in distinct patterns uniquely created by the disloc model.

Differences between thrust and normal fault traces were minimal in edge maps created from disloc data, but noise patterns created for strike slip faults were slightly different.

Disloc3 also enabled us to model our area of interest. A synthetic interferogram was created by modeling the cataloged CGS fault system in our study area and their triggered motions during the El Mayor-Cucapah earthquake. This model also included simulated motion along the main earthquake fault, which lay outside our area of study. The edge-detection code was able to identify all of the faults from the synthetic interferogram (Figure 19).

As a proof of concept for the methodology in an earthquake situation a large earthquake was imagined occurring on the Yuha Fault, which is located within the control area. The area used for this was a UAVSAR strip of coseismic slip from the El Mayor Cucapah earthquake from which the Yuha Fault was discovered. The edge detection code was used to identify the fault to be used as a line source. The edge map was optimized to isolate the fault trace and georeferenced to the polygon area from which it was taken. Using E-DECIDER's KML Generator service, a risk assessment map was generated for a 50 kilometer radius around the line source creating a map of infrastructure that was at potential risk for damage from the earthquake displacement (Figure 20). This would not apply to the UAVSAR image collection or subsequent data processing necessary to reach this step in the hazard response process. Data collection and processing are the two most time consuming portions of the process due to the logistics of reaching the UAVSAR plane, the time it takes to gather the data, transport it, and perform numerous processing steps on a large body of data. However, it confirms that this methodology can be used to identify movement along secondary faults in an active hazard area and identify infrastructure at risk of damage from secondary fault movement using UAVSAR data.

Errors & Uncertainty:

Uncertainty in detecting a fault lies partially with the inability to know whether the entire length of the fault is being detected from the edge map alone. A fair amount of confidence can be applied to the edge map when georeferenced and compared to the area of the InSAR from which it was taken. In this way a visual analysis can be used to determine whether the code is detecting all of the motion that is visible within the interferogram. However, that does not necessarily mean that deformation occurring along the entire length of the fault has been revealed by the InSAR. It also needs to be determined what size fault displacements are filtered out in relation to threshold levels-- then it can be stated with confidence that the edge code detected faults with displacement *greater than* some value. This would require a large sample size of UAVSAR images of a range of faults of varying displacement values to establish a correlation curve.

An additional uncertainty is related to fault strike of strike-slip faults. If the fault lies perpendicular to the LOS, the strike-slip motion will not appear in the interferogram. Thus, to confidently detect all motion, 2 interferograms covering the same area but with perpendicular LOS should be created.

There are a regular set of noise sources which it has been difficult to remove. These include rivers, stream beds, roads, and agricultural areas especially. In the case of agricultural areas, they have often been left out entirely at the processing stage; however, this creates a barrier to fault detection in these areas. This has been revealed

in an agricultural area in which fault movement occurred during the El Mayor Cucapah earthquake, but the fault itself is difficult to distinguish due to the noise created by the agricultural zones. The noise is a result of the feature having data values above the upper threshold of the algorithm and in most cases higher than the values of the faults. For this reason, it has been suggested that a third threshold be added to the fault detection algorithm to stop edge detection above a certain threshold value to create a window in which faults would be preferentially detected.

Another source of error that was unexpected was that created by extensive data dropout. Data dropout in some cases occurs along the faults, which has led to inability of the detection algorithm to see the fault well or at all some areas. The result is generally noisy when distinguishable or segmented. This may be considered one drawback to this application of edge detection; however, it is only applicable to a small number of cases.

Future Work:

The fault edge-detection algorithm can be further improved by integrating a slip calculation feature that measures the slip corresponding to the InSAR image time period. Furthermore, the fault detection algorithm usage can be expanded by having it made compatible with all InSAR data, not just UAVSAR data.

Since the modeling tool is not dependent on the occurrence of an event, it would be interesting to apply this method to earthquake predictions. One could model these predicted scenarios for a range of parameters on known faults creating synthetic interferogram images. The risk assessment tools and techniques could then be employed to project damage scenarios much like the exercises that have been completed by this projects partner organizations.

The fault detection algorithm can be further improved by integrating a slip calculation feature that measures the slip corresponding to the interferogram time period. This would enable the creation of tilt/deformation maps from the UAVSAR data itself. This would thereby streamline the number of resources needed to create tilt/deformation maps, risk assessment maps, and fault edge detection maps. Furthermore, the fault detection algorithm can expand its usage by having it be compatible with all radar interferogram data, not just UAVSAR data.

Conclusions

UAVSAR and other Earth Observations Systems are powerful tools for observing and understanding earthquake systems. The implementation of these tools has great potential for earthquake response and earthquake hazard mitigation to infrastructure and property in the densely populated state of California.

The edge-detection algorithm can reliably detect faults with earthquake-rupture or earthquake-triggered movement in UAVSAR-derived InSAR data; however, creeping faults cannot be detected. Further refinement to reduce the noise will be necessary for full automation of this process.

Agencies and researchers can use the detected faults to develop more complete models, simulations, and maps that increase understanding of earthquakes. In turn, an improved understanding of earthquakes along with the detection algorithm to identify fault motion will improve the effectiveness with which first responders and disaster managers can react to an earthquake. This will lead to more complete

methods being used for earthquake hazard assessment, mitigation, response, and recovery. A better understanding of these fault systems will ultimately help alleviate the ever-present earthquake risks and hazards for the millions of California residents.

Acknowledgments

We would like to thank our science advisors, Margaret Glasscoe, Jay Parker, and mentor Benjamin Holt for their guidance and support.

References

- Alaska Satellite Facility, 2013. SAR Data Center Data: Alaska Satellite Facility.
<http://www.asf.alaska.edu/program/sdc/data0>
- Canny, J. A., 1986, Computational Approach to Edge Detection: IEEE Transactions on Pattern Analysis and Machine Intelligence 8(6), p. 679-698.
- Hensley, S.; Zebker, H.; Jones, C.; Michel, T.; Muellerschoen, R. & Chapman, B., 2009, First Deformation Results Using the NASA/JPL UAVSAR Instrument: IEEE Aerospace and Electronic Systems Magazine, p. 1051 - 1055.
- Naranjo, L., November 20, 2011, Baja's Fault: EOSDIS website,
<http://earthdata.nasa.gov/featured-stories/featured-research/bajas-fault>
(accessed July 1, 2013)
- QuakeSim, 2011. About: Quakesim website, quakesim.org/about (accessed July 3, 2012)
- Rosen, P., June 16, 2008, Principles and Theory of Radar Interferometry: UNAVCO Short Course, Jet Propulsion Laboratory, http://www.grss-ieee.org/wp-content/uploads/2010/06/Radar_Interferometry_Part1.pdf (accessed June 4, 2013).
- Rosen, P., Hensley, S.; Wheeler, K.; Sadowy, G.; Miller, T.; Shaffer, S.; Muellerschoen, R.; Jones, C.; Madsen, S. & Zebker, H., 2007, UAVSAR: New NASA Airborne SAR System for Research: Aerospace and Electronic Systems Magazine, IEEE 22(11), p. 21-28.
- Rymer, Michael J. et al., 2010, Triggered Surface Slips in Southern California Associated with the 2010 El Mayor-Cucapah, Baja California, Mexico, Earthquake: U.S. Geological Survey Open-File Report 2010 - 1333 (digital copy, 72 p.)
- Toan, T. L., September 3, 2007, Introduction to SAR Remote Sensing: Advanced Training Course on Land Remote Sensing, European Space Agency,
<http://earth.esa.int/landtraining07/D1LA1-LeToan.pdf> (accessed June 4, 2013).
- Jun Wang; Pierce, M.; Yu Ma; Fox, G.; Donnellan, A.; Parker, J. & Glasscoe, M., 2012, Using Service-Based GIS to Support Earthquake Research and Disaster Response: Computing in Science and Engineering 14(5), p. 21-30.
- Wei, M., Sandwell, D.; Fialko, Y. & Bilham, R., 2011, Slip on faults in the Imperial Valley triggered by the 4 April 2010 Mw 7.2 El Mayor-Cucapah earthquake revealed by InSAR: Geophysical Research Letters (38), p. 1- 6.
- Wei Shnengji., Fielding, E.; Leprince, S.; Sladen, A.; Avouac, J.-P.; Helmberger, D.; Hauksson, E.; Risheng Chu; Simons, M.; Hudnut, K.; Herring, T. & Briggs, R., 2011, Superficial simplicity of the 2010 El Mayor-Cucapah earthquake of Baja California in Mexico: Nature Geoscience (4), p. 615-618.

Appendices

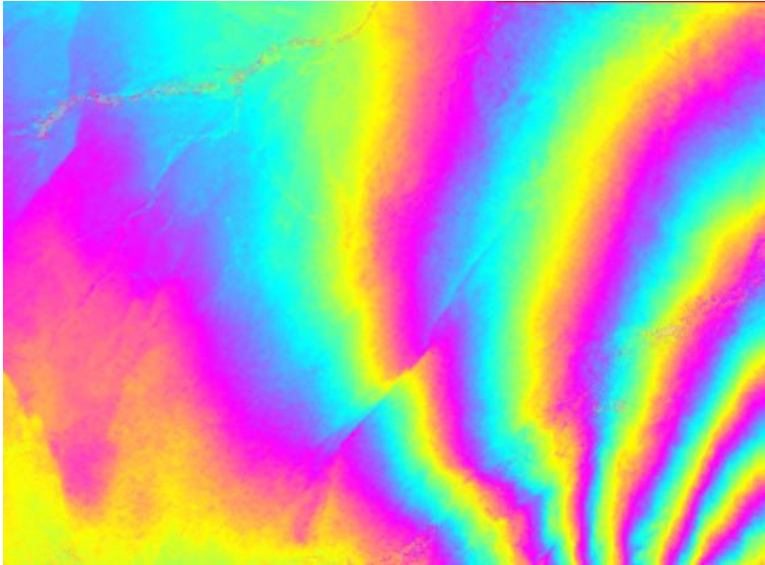


Figure 5. InSAR of the primary study area of PolySel2 polygon within coseismic InSAR image taken of the El Mayor Cucapah Earthquake in 2010.

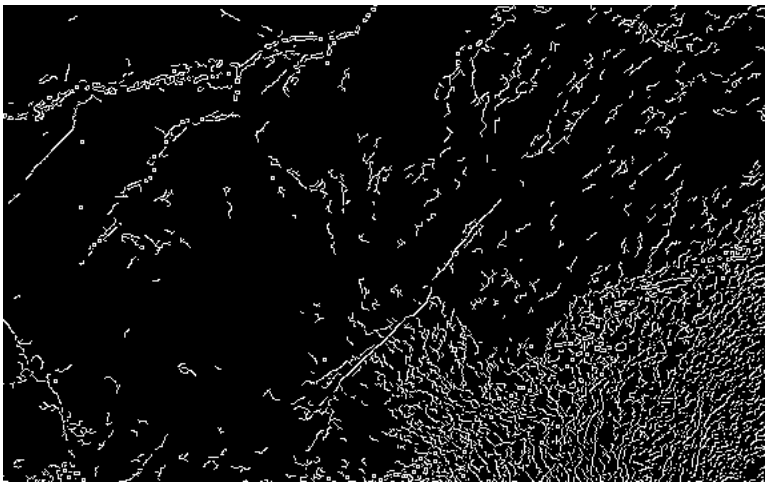


Figure 6. Edge map created with elevated high threshold setting in PolySel area and InSAR of coseismic slip from the El Mayor Cucapah earthquake.



Figure 7. Edge map created with elevated low threshold ratio setting in PolySel area and InSAR of coseismic slip from the El Mayor Cucapah Earthquake.

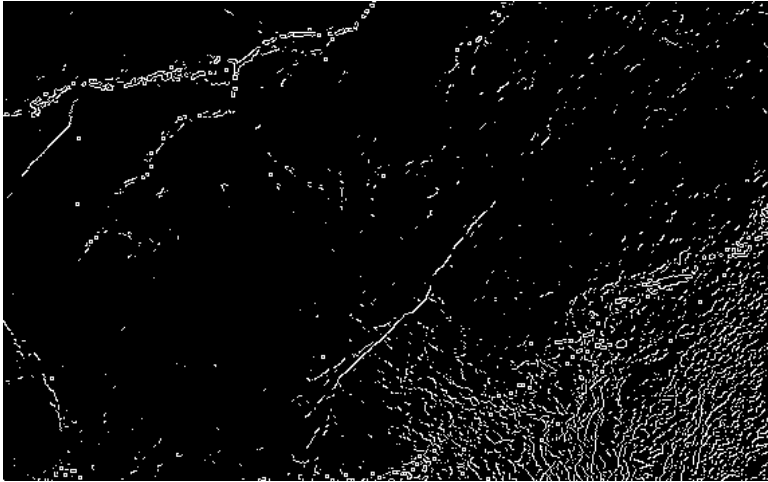


Figure 8. Edge map image created from polygon PolySel2 and interferogram of coseismic slip following the El Mayor Cucapah earthquake.

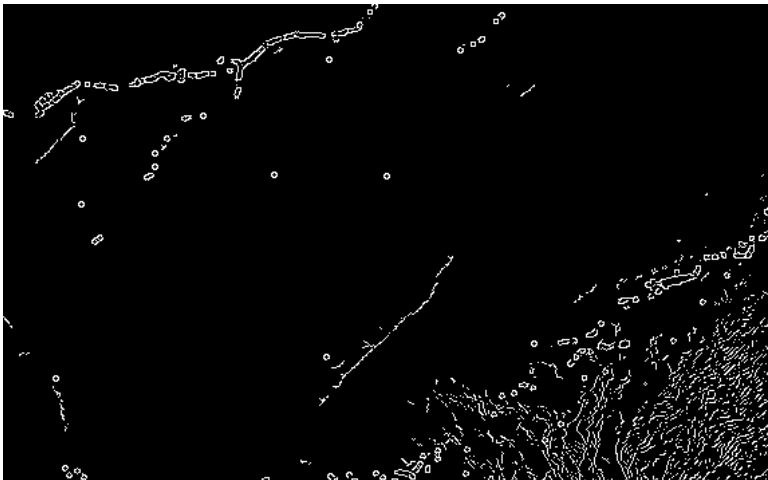


Figure 9. Edge map with increased smoothing coefficient. PolySel2 area and InSAR of coseismic slip following the El Mayor Cucapah earthquake.

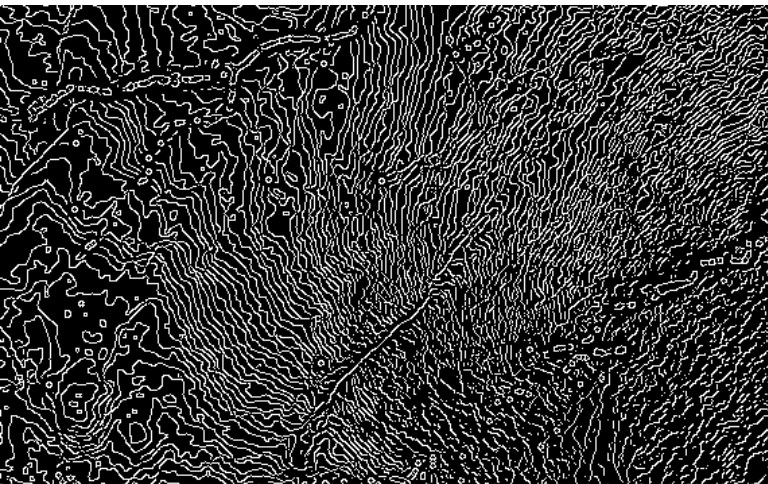


Figure 10. Edge map with aperture increased to value 7. Produced from PolySel2 and InSAR of coseismic slip from the El Mayor Cucapah earthquake.

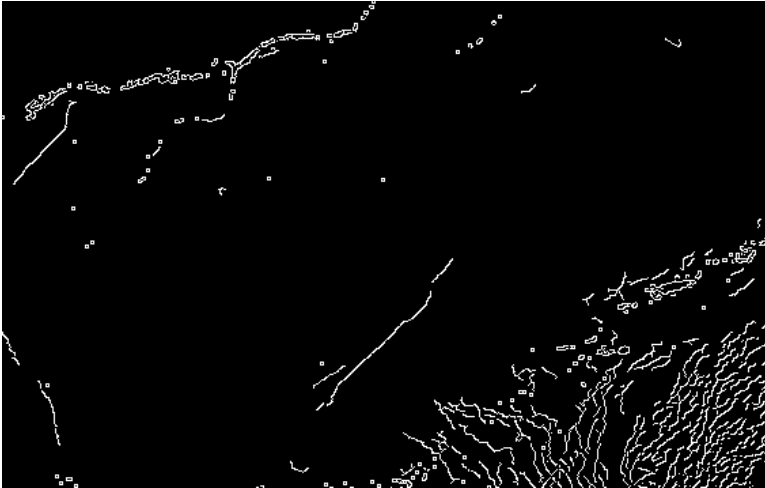


Figure 11. Edge map of the PolySel area and InSAR of coseismic slip from the El Mayor Cucapah earthquake with optimized parameters: aperture 5, smoothing coefficient 4, high threshold 18, low threshold 65% of high threshold.

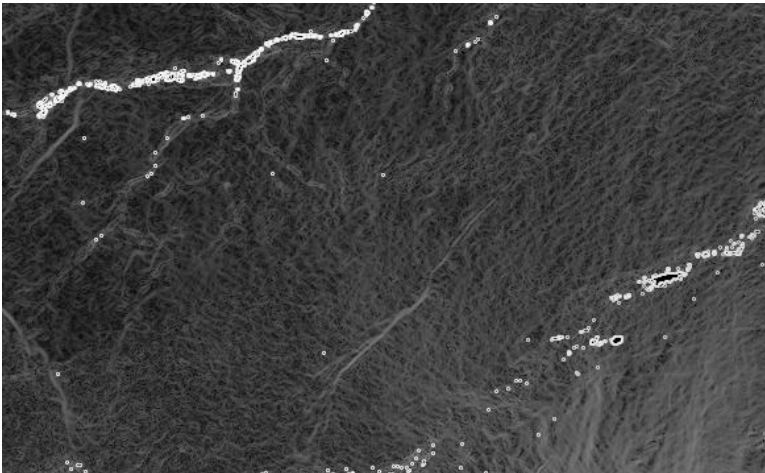


Figure 12. Image created by the Logarithm of the Magnitude of the Gradient of the Phase from InSAR data. Created by the edge detection algorithm from PolySel2 polygon and InSAR image of coseismic slip following the El Mayor Cucapah Earthquake.

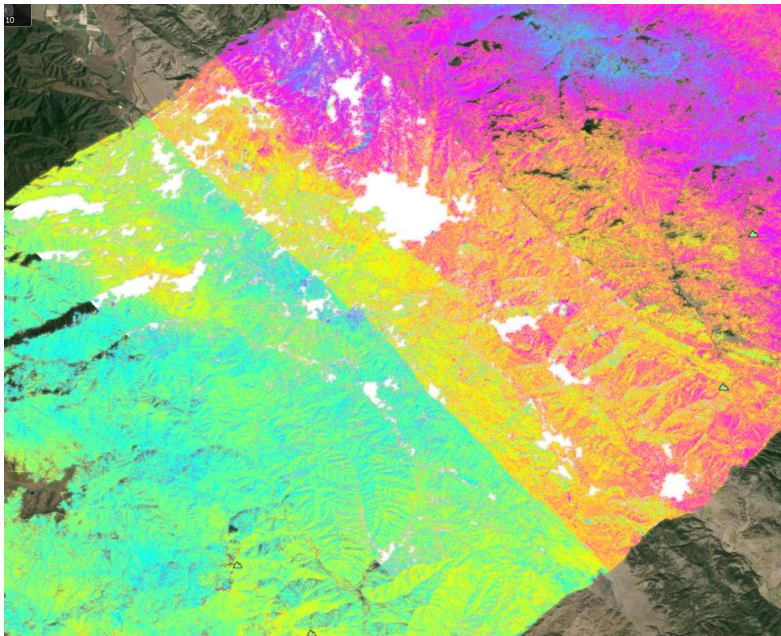


Figure 13. InSAR of creeping portion of the San Andreas Fault. White portion indicates borders of polygon area used for processing, it also serves to accentuate extent of data dropout in the image.

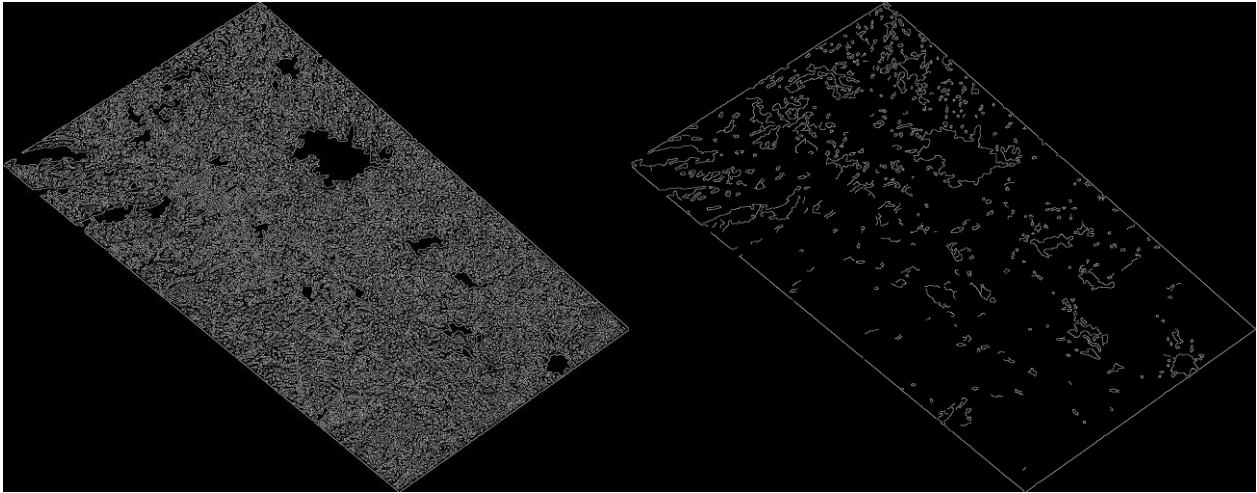


Figure 14. (Left) Edge map processed with default algorithm settings. Edges difficult to see, but the fault that was clearly visible in the InSAR is difficult to find. (Right) Edge map created with elevated upper threshold and smoothing coefficient to bring out the fault trace. Instead, what's left is large portions of noise and evidence of the data dropout.

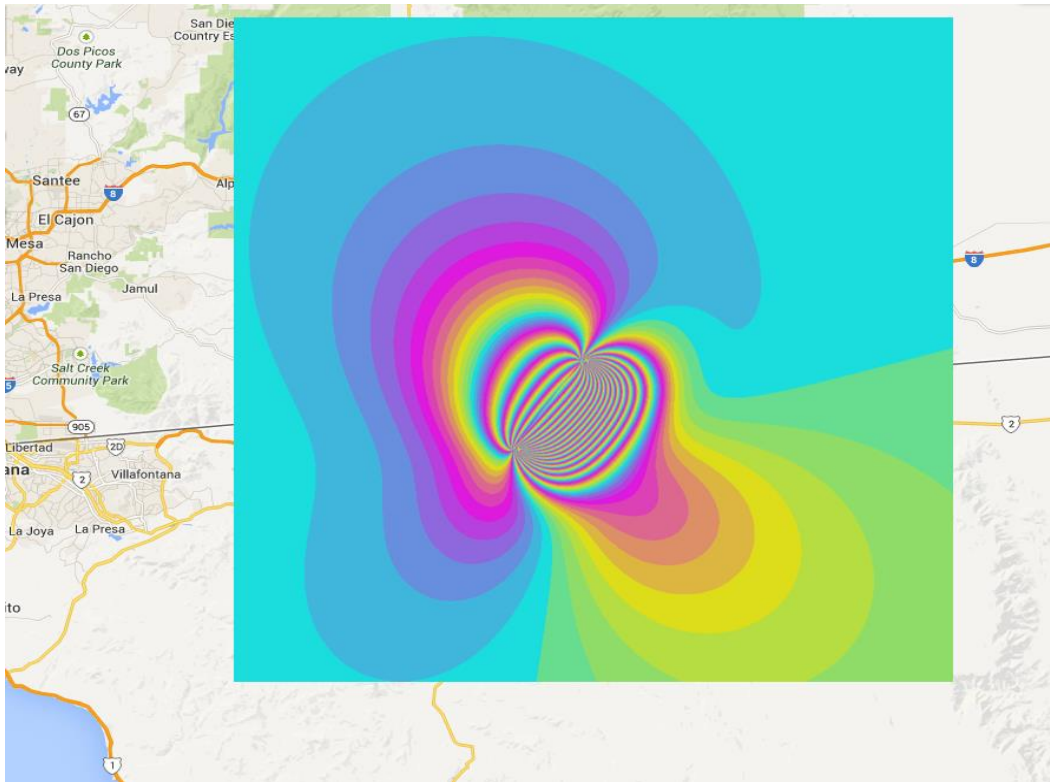


Figure 15. Example synthetic InSAR created in Disloc3 elastic forward model. Image taken in Disloc Portal.

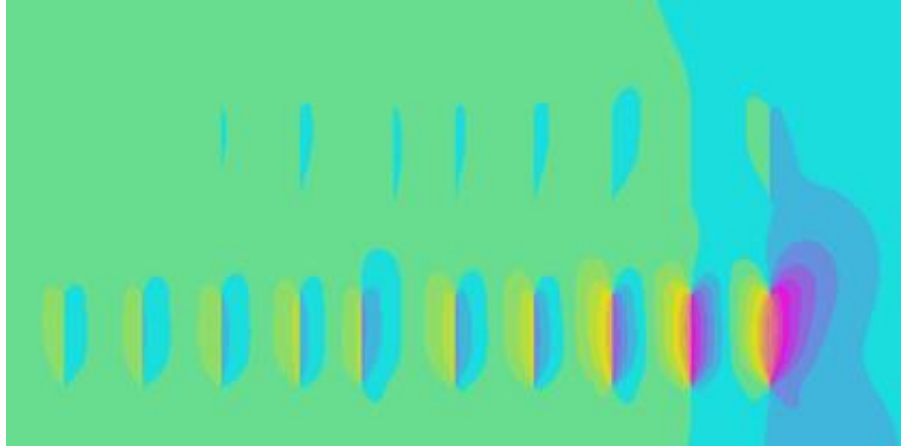


Figure 16. Synthetic InSAR created in Disloc for an array of faults used to test the effects of displacement values on edge detection algorithm.

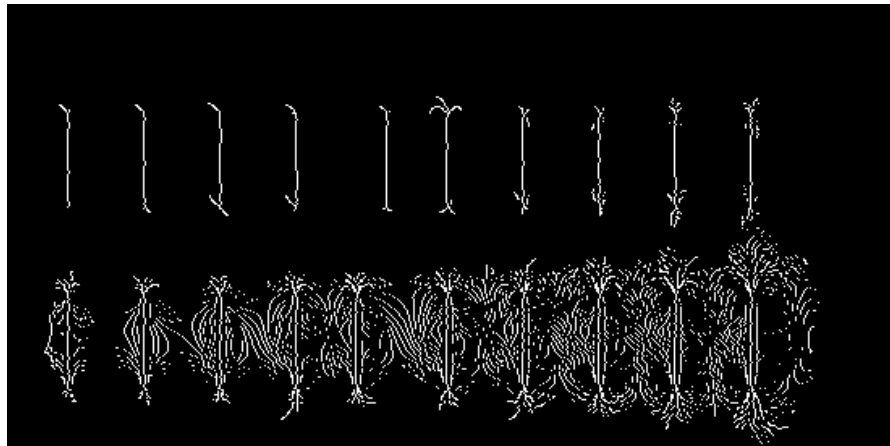


Figure 17. Edge map created from array of faults modeled in Disloc to test effects of displacement values on edge detection algorithm.



Figure 18. Pair of images showing the effects of variations in strike (orientation) on the edge detection algorithm. The faults in this image were modeled in Disloc sharing the same displacement values and geometries but different strikes.

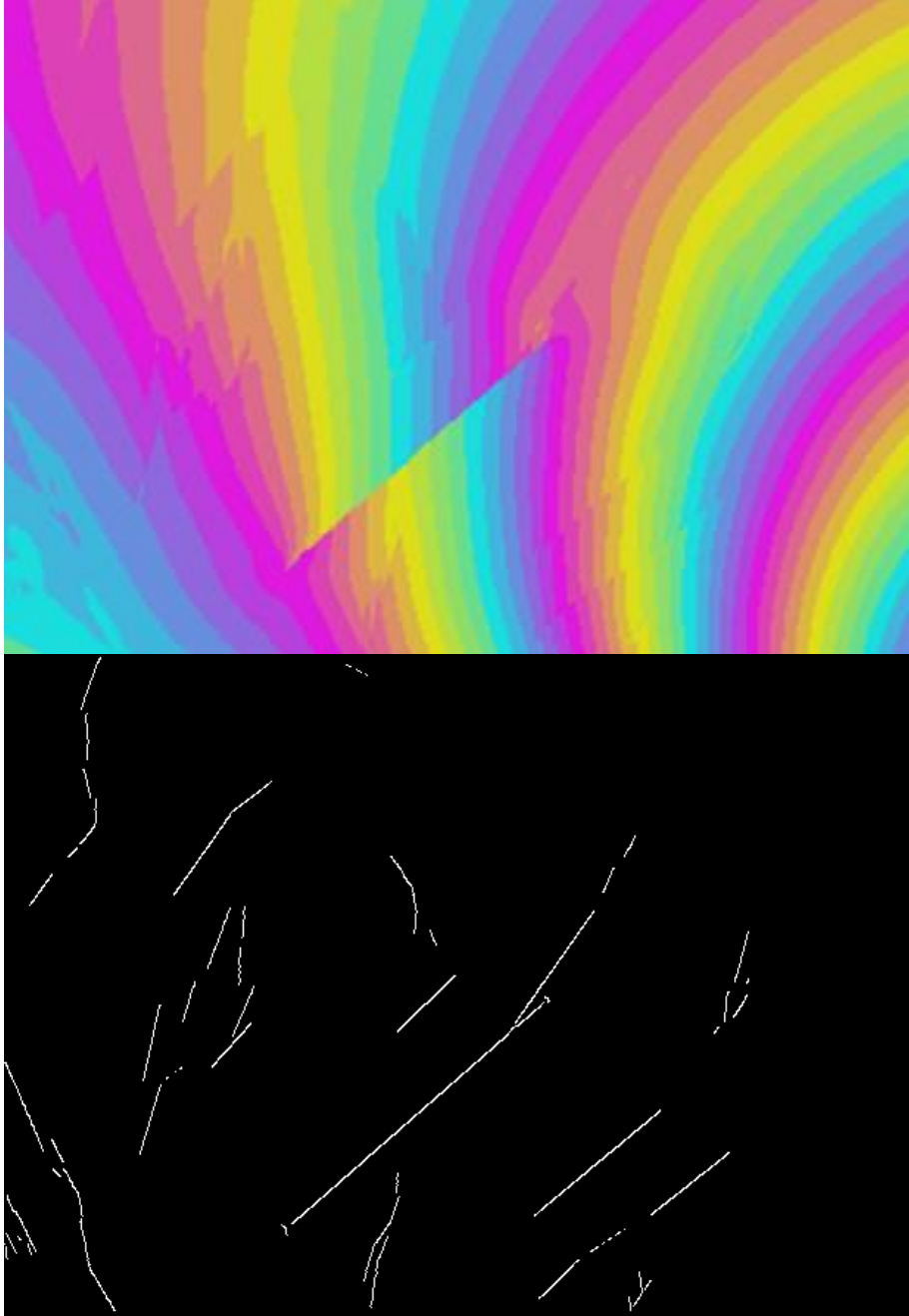


Figure 19. The top image shows the synthetic interferograms model created by Disloc for our area of study. The bottom image is the edge-detection code results for the synthetic interferogram.

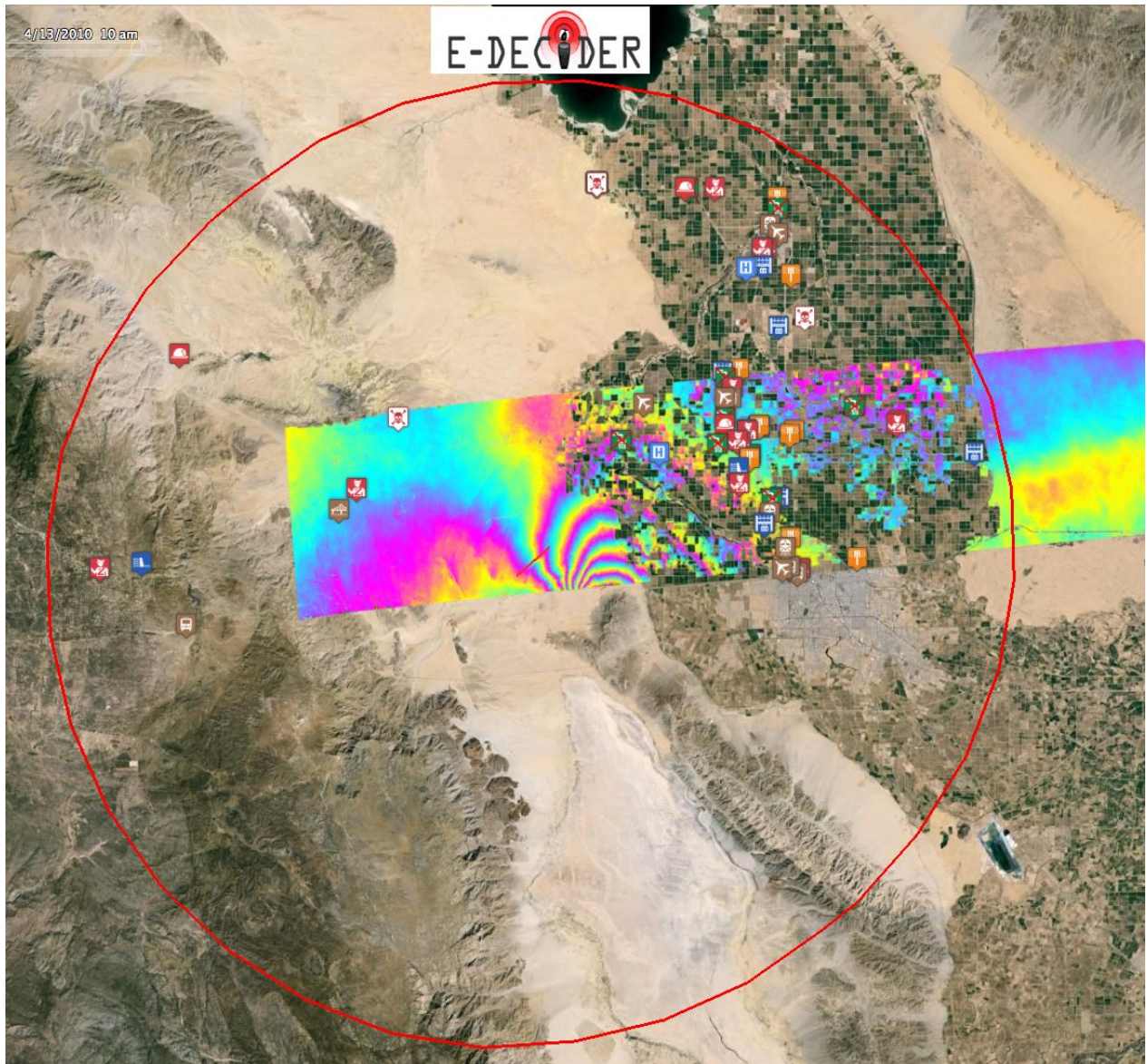


Figure 20. This image, taken in Google Earth, is an example of a finite fault event occurring on the Yuha Fault in the Imperial Valley of Southern California. E-DECIDER's KML generation service was used to create the risk assessment map and utilities overlay.

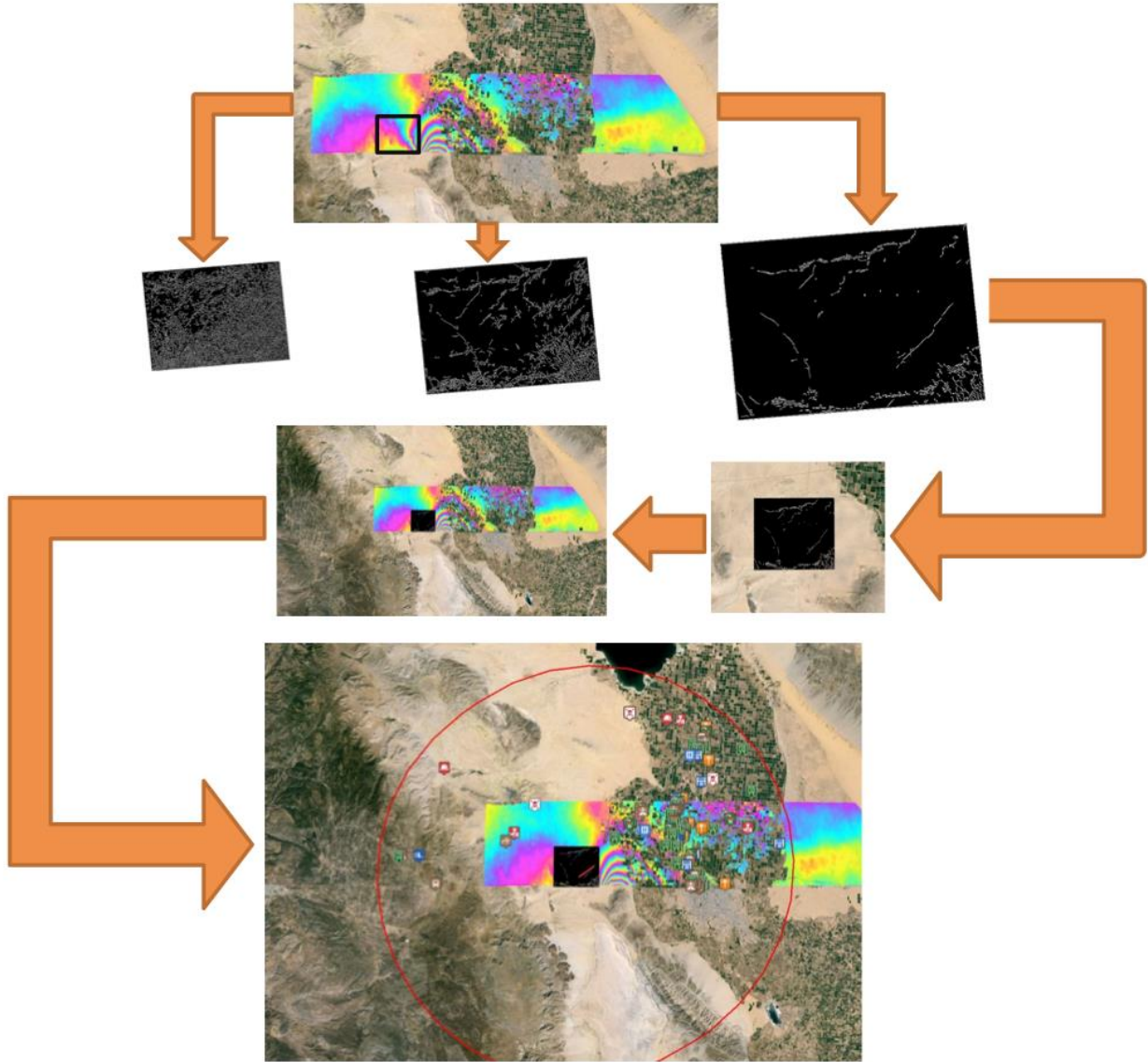


Figure 21. Flowchart of steps taken to optimize an edge map from an area of InSAR data, georeference the edge map, and produce a risk assessment map using E-DECIDER's KML generator service.